



# Nitrogen contained rhodium nanosheet catalysts for efficient hydrazine oxidation reaction

Jie Shi<sup>a,1</sup>, Qintao Sun<sup>a,1</sup>, Jinxin Chen<sup>a</sup>, Wenxiang Zhu<sup>a</sup>, Tao Cheng<sup>a</sup>, Mengjie Ma<sup>a</sup>, Zhenglong Fan<sup>a,\*</sup>, Hao Yang<sup>a,\*</sup>, Fan Liao<sup>a,\*</sup>, Mingwang Shao<sup>a,\*</sup>, Zhenhui Kang<sup>a,b,\*\*</sup>

<sup>a</sup> Institute of Functional Nano & Soft Materials (FUNSOM), Jiangsu Key Laboratory for Carbon-Based Functional Materials & Devices, Soochow University, 199 Ren'ai Road, Suzhou 215123, Jiangsu, China

<sup>b</sup> Macao Institute of Materials Science and Engineering (MIMSE), MUST–SUDA Joint Research Center for Advanced Functional Materials, Macau University of Science and Technology, Taipa 999078, Macao Special Administrative Region of China

## ARTICLE INFO

### Keywords:

Metastable-phase

Rhodium

Electrocatalysis

Hydrazine oxidation reaction

## ABSTRACT

The hydrazine oxidation reaction (HzOR) has been considered as a more energy-efficient alternative to the oxygen evolution reaction in water electrolysis. To design efficient electrocatalysts for HzOR, precise engineering of materials is required to increase active sites and build electronic structures. Herein, nitrogen contained face-centered cubic rhodium (N-fcc-Rh) nanosheets are prepared by directly annealing metastable trigonal rhodium oxide precursor in the ammonia atmosphere. Benefiting from the abundant active sites and unique electronic structure, the optimal N-fcc-Rh-300 electrocatalyst achieves an ultra-low working potential of  $-81$  mV (vs. RHE) at  $10 \text{ mA cm}^{-2}$  in  $1.0 \text{ M KOH}/0.5 \text{ M N}_2\text{H}_4$ . Density functional theory calculations suggest the N element in the N-fcc-Rh electrocatalyst enables to the reduction of the formation energy of the potential-determining step from  $^*\text{NH}_2\text{NH}_2$  to  $^*\text{NHNH}_2$  for the HzOR process. This work reveals a new strategy to prepare advanced metal electrocatalysts for various electrochemical applications.

## 1. Introduction

The preparation of hydrogen ( $\text{H}_2$ ) from water electrolysis has a history of over 200 years, while traditional anodic oxygen evolution reaction ( $\text{OER}$ ,  $4\text{OH}^- \rightarrow \text{O}_2 + 2 \text{H}_2\text{O} + 4\text{e}^-$ ) with the kinetically sluggish four-electron process has become an enormous challenge for its further practical application [1–8]. Hydrazine oxidation reaction (HzOR,  $\text{N}_2\text{H}_4 + 4\text{OH}^- \rightarrow \text{N}_2 + 4 \text{H}_2\text{O} + 4\text{e}^-$ ) has a lower theoretical thermodynamic oxidation potential ( $-0.33 \text{ V}$  vs. RHE) in comparison to the conventional OER process ( $1.23 \text{ V}$  vs. RHE), making it a more energy-efficient process [9–16]. More importantly,  $\text{N}_2\text{H}_4$  only generates  $\text{N}_2$  during the oxidation process, which can effectively avoid the explosion caused by the mixing of the final products ( $\text{H}_2$  and  $\text{O}_2$ ) from the traditional electrochemical water splitting [17–20]. In addition, the structure-activity relationships have not been explained well in the HzOR to date, which are mainly attributed to its complex reaction process [21–23]. Therefore, it is

essential to develop an efficient HzOR electrocatalyst with extraordinary activity, long-term stability and clear structure-activity relationships.

Rhodium (Rh), as a member of Pt-group metals, has attracted extensive attention due to its similar physicochemical properties to Pt [24,25]. Given the high price and scarcity of the noble metal Rh, more attention should be paid to finding material optimization strategies to improve its catalytic activity and atomic utilization efficiency. On this basis, many previous works have greatly improved the catalytic activity of Rh-based electrocatalysts, including control of the morphology [26, 27], synthesis of polymetallic alloy [28,29], and introduction of crystal defects and lattice strain [30–32]. In addition to the above feasible strategies, the introduction of non-metallic elements (such as N, S, and P) into metallic electrocatalysts also gives a possibility to improve electrocatalytic activity by regulating its electronic structure [33–39]. However, the description of the interaction between non-metallic elements and metals remains unclear.

\* Corresponding authors.

\*\* Corresponding author at: Institute of Functional Nano & Soft Materials (FUNSOM), Jiangsu Key Laboratory for Carbon-Based Functional Materials & Devices, Soochow University, 199 Ren'ai Road, Suzhou 215123, Jiangsu, China.

E-mail addresses: [zlfan@suda.edu.cn](mailto:zlfan@suda.edu.cn) (Z. Fan), [haoyang@suda.edu.cn](mailto:haoyang@suda.edu.cn) (H. Yang), [fliao@suda.edu.cn](mailto:fliao@suda.edu.cn) (F. Liao), [mwshao@suda.edu.cn](mailto:mwshao@suda.edu.cn) (M. Shao), [zhkang@suda.edu.cn](mailto:zhkang@suda.edu.cn) (Z. Kang).

<sup>1</sup> J Shi and QT Sun contributed equally.

Inspired by these possibilities, we synthesized an ultrathin 2D nitrogen contained face-centered cubic Rh nanosheets (N-fcc-Rh) by direct annealing metastable trigonal Rh oxide (Tri-RhO<sub>2</sub>) precursor in the ammonia (NH<sub>3</sub>) atmosphere. The ultra-thin 2D morphology of N-fcc-Rh exposes more active sites. By introducing the N elements, the surface electronic structure was adjusted, further improving the catalytic activity. As expected, the optimal N-fcc-Rh-300 delivers an ultra-low working potential of  $-81$  mV (vs. RHE) to reach the current density of  $10 \text{ mA cm}^{-2}$  in  $1.0 \text{ M KOH}/0.5 \text{ M N}_2\text{H}_4$  electrolyte with a small Tafel slope of  $14.1 \text{ mV dec}^{-1}$ . Notably, the working potential only shifts  $35 \text{ mV}$  at  $10 \text{ mA cm}^{-2}$  after a  $72 \text{ h}$  stability test for the optimal N-fcc-Rh-300, revealing its superior long-term durability and stability. Density functional theory (DFT) calculations suggest that introducing N elements into metallic Rh leads to a noticeable shift of the *d*-band center, adjusting the surface electronic structure thereby offering suitable adsorption/desorption capacity toward the key reaction intermediate of the HzOR process. This work opens a new route to synthesize efficient electrocatalysts by introducing non-metallic elements into metal materials.

## 2. Experimental section

### 2.1. Materials

Rhodium (III) chloride hydrate (RhCl<sub>3</sub>·3H<sub>2</sub>O), potassium hydroxide (KOH, 99 %), 10 % Rh/C and 20 % Pt/C were bought from Shanghai Macklin Biochemical Co. Isopropanol (99.8 %) was obtained from Shanghai Titan Technology Co. Nafion ionomer (5.0 wt%) was bought by Shanghai Universal Biotech Co. All the reagents were used directly without further purification.

### 2.2. Synthesis of Tri-RhO<sub>2</sub> nanosheets

As reported in previous work, the metastable Tri-RhO<sub>2</sub> nanosheets were prepared via a one-step strategy [40]. Briefly,  $10 \text{ g}$  KOH and  $300 \text{ mg}$  RhCl<sub>3</sub>·3 H<sub>2</sub>O were added into a corundum crucible and ground for half an hour. And then, the mixed solid was calcined in the air atmosphere ( $700^\circ\text{C}$  for  $2 \text{ h}$ ,  $10^\circ\text{C min}^{-1}$ ). After cooling down to room temperature, the resulting sample was washed with  $1 \text{ M}$  HCl several times to remove the impurity, then the above product was cleaned again by using redistilled water to maintain pH = 7. Then the above product was further dried at  $60^\circ\text{C}$  for  $12 \text{ h}$  to obtain final metastable Tri-RhO<sub>2</sub> nanosheets.

### 2.3. Synthesis of N-fcc-Rh nanosheets

To obtain N-fcc-Rh nanosheets, the as-prepared Tri-RhO<sub>2</sub> catalyst was calcined in the NH<sub>3</sub> flow ( $65 \text{ sccm}$ ) ( $300^\circ\text{C}$  for  $2 \text{ h}$ ,  $10^\circ\text{C min}^{-1}$ ) [41–43]. After cooling down to room temperature, the black powder product, N-fcc-Rh-300, was obtained. The Tri-RhO<sub>2</sub> precursor was also annealed at  $200^\circ\text{C}$ ,  $250^\circ\text{C}$ ,  $350^\circ\text{C}$ , and  $400^\circ\text{C}$  to obtain N-fcc-Rh-200, N-fcc-Rh-250, N-fcc-Rh-350 and N-fcc-Rh-400, respectively.

### 2.4. Catalyst characterization

The details of the catalyst characterization and DFT calculation are described in [Supporting Information](#).

## 3. Results and discussion

### 3.1. Formation and morphological characterizations of and Tri-RhO<sub>2</sub> and N-fcc-Rh nanosheets

The N-fcc-Rh nanosheets were synthesized by direct annealing metastable Tri-RhO<sub>2</sub> nanosheet precursor in the NH<sub>3</sub> atmosphere (Fig. S1). The Tri-RhO<sub>2</sub> nanosheet precursor was synthesized by a

bottom-up strategy and its powders show brown color (Fig. S2a) [40]. From the X-ray powder diffraction (XRD) pattern in Fig. S3a and S4a, the metastable phase RhO<sub>2</sub> precursor can be determined as a trigonal phase [40]. The scanning electron microscope (SEM) image and transmission electron microscope (TEM) image of Tri-RhO<sub>2</sub> are shown in Figs. S3b and S3c. The morphology of Tri-RhO<sub>2</sub> is a rigid lamellar structure and the diameter of Tri-RhO<sub>2</sub> ranges from  $100$  to  $500 \text{ nm}$ . As displayed in Figs. S3d and S3e, scanning transmission electron microscopy (STEM) image and selected area electron diffraction (SAED) pattern of Tri-RhO<sub>2</sub> further indicate its trigonal crystal structure. The X-ray photoelectron spectroscopy (XPS) spectrum of Rh 3d for Tri-RhO<sub>2</sub> shows that the two peaks at  $309.35$  and  $314.26 \text{ eV}$  are ascribed to Rh 3d<sub>5/2</sub> and Rh 3d<sub>3/2</sub> of Rh<sup>4+</sup>, respectively (Fig. S3f) [44].

After annealing Tri-RhO<sub>2</sub> precursor at  $300^\circ\text{C}$  in the NH<sub>3</sub> atmosphere, the obtained product of N-fcc-Rh-300 nanosheet powders display black color (Fig. S2b). As shown in Fig. 1a, the peaks of the N-fcc-Rh-300 are highly consistent with the standard card (JCPDS No. 01-1214) of metallic Rh without other peaks from impurities (see more details in SI, Fig. S4b). As can be seen from Figs. 1b and 1c, SEM and TEM images show that the product of N-fcc-Rh still maintains 2D nanosheet morphology, which originate from 2D Tri-RhO<sub>2</sub> precursor nanosheets. Moreover, the XRD patterns of N-fcc-Rh at different annealing temperatures ( $200$ ,  $250$ ,  $350$  and  $400^\circ\text{C}$ ) were collected in Fig. S5 and Fig. S6. The SEM images of N-fcc-Rh at different annealing temperatures ( $200$ ,  $250$ ,  $350$  and  $400^\circ\text{C}$ ) were collected in Fig. S7, these samples also exhibit 2D nanosheet morphology. There are two possible ways in which N atoms exist in catalysts. One is N atoms enter the lattice gap [41,45,46], and the other is N atoms replace metal atoms (as schematic shown in Fig. 1d) [47]. Although we do not know the exact existence site of N in Rh, the introduction of the N element does not change the face-centered cubic structure of metallic Rh as confirmed by XRD pattern in Fig. 1a. Energy dispersive X-ray spectroscopy (EDX) spectrum of N-fcc-Rh-300 clearly shows only two elements of Rh and N can be detected without other impurities, and one can see that the molar ratio of Rh and N is close to  $9:1$  (Figs. S8 and S9).

The thickness of N-fcc-Rh-300 nanosheets is determined to be only  $3.1 \text{ nm}$ , revealed by an atomic force microscope (AFM) image (Fig. 2a), further reflecting its ultrathin nanosheet structure. The lattice spacings of  $2.20$  and  $1.92 \text{ \AA}$  are assigned to the (111) and (200) crystal planes of metallic Rh in the high-resolution TEM image in Fig. 2b. The included angle of the two crystal planes is  $54.7^\circ$ . The XPS spectrum in Fig. 2c further demonstrates that the high-purity metallic Rh was synthesized and  $307.59$  and  $311.92 \text{ eV}$  peaks can be ascribed to Rh<sup>0</sup> 3d<sub>5/2</sub> and Rh<sup>0</sup> 3d<sub>3/2</sub>, respectively [48], which are different from those of Tri-RhO<sub>2</sub>. More importantly, the N 1s XPS spectrum of N-fcc-Rh-300 was illustrated in Fig. 2d, the peak at  $397.81 \text{ eV}$  is attributed to Rh-N [42]. In order to exclude that the N element may derive from adsorbed NH<sub>3</sub> during the annealing process, the XPS spectra of N-fcc-Rh-300 were again collected after soaking it in  $1 \text{ M}$  HCl solution for  $24 \text{ h}$ . As can be seen from Fig. S10, the signal of the N element still can be observed at the XPS spectrum, indicating that the N element has been successfully inserted into the lattice of metallic Rh. In conclusion, the above results reflect that the N-fcc-Rh-300 nanosheets were perfectly prepared by direct annealing Tri-RhO<sub>2</sub> nanosheet precursor in the NH<sub>3</sub> atmosphere.

### 3.2. The electrochemical performance of N-fcc-Rh-300 electrocatalyst

In this part, the HzOR activity of the N-fcc-Rh-300 electrocatalyst was evaluated in  $1.0 \text{ M KOH}/0.5 \text{ M N}_2\text{H}_4$  electrolyte by a three-electrode system. As shown in Fig. S11, the Hg/HgO electrode was calibrated before the electrochemical test. To intuitively reflect the HzOR activity of N-fcc-Rh-300, the linear sweep voltammetry (LSV) curves of N-fcc-Rh in  $1.0 \text{ M KOH}$  electrolyte containing different N<sub>2</sub>H<sub>4</sub> concentrations were collected (Fig. 3a). The HzOR performance of the N-fcc-Rh-300 electrocatalyst is improved with the increase of the concentration of N<sub>2</sub>H<sub>4</sub>, and there is almost no HzOR activity in  $1 \text{ M KOH}$

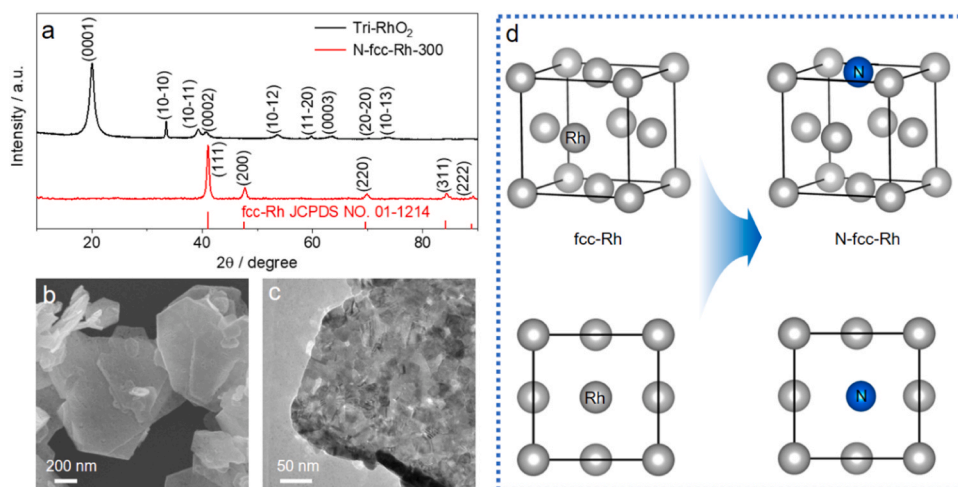


**Fig. 1.** (a) XRD profiles of N-fcc-Rh-300 and Tri-RhO<sub>2</sub>. (b) SEM, (c) TEM images of N-fcc-Rh-300. (d) Schematic structures of fcc-Rh and N-fcc-Rh, where silver and blue balls represent Rh and N, respectively.

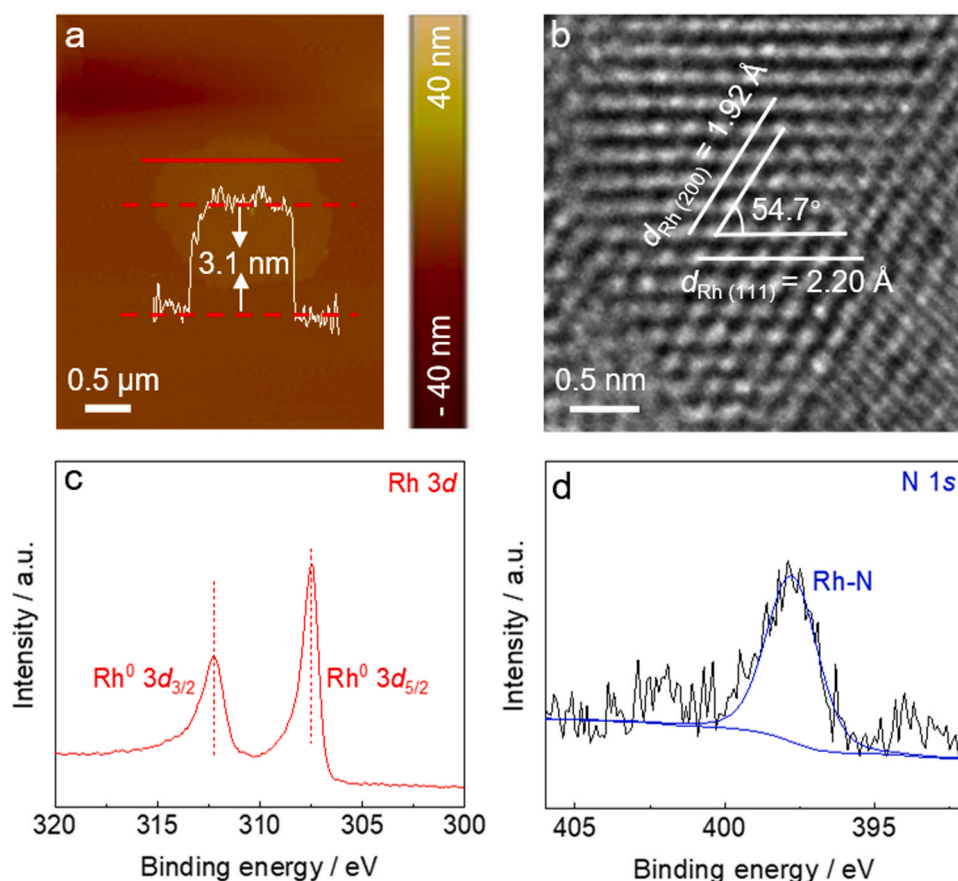


**Fig. 2.** (a) AFM image of N-fcc-Rh-300. (b) HRTEM images of N-fcc-Rh-300. XPS spectra for N-fcc-Rh-300: (c) Rh 3d and (d) N 1s.

electrolyte without N<sub>2</sub>H<sub>4</sub>. The HzOR performance of N-fcc-Rh at different annealing temperatures is shown in Figs. 3b and 3c, the N-fcc-Rh-300 exhibits the best HzOR performance. In addition, the N-fcc-Rh-300 also exhibits the smallest Tafel slope (Fig. S11). In addition, the N/Rh atomic ratio was determined by the EDX spectra, and then the correlation between the N/Rh atomic ratio, HzOR performance and annealing temperatures was established. As shown in Fig. 3d, the N/Rh atomic ratio of N-fcc-Rh increases with the increase of annealing temperatures, indicating the excellent activity of rich N contained fcc-Rh for

HzOR.

Fig. 4a shows the LSV curves of N-fcc-Rh-300, Tri-RhO<sub>2</sub>, Pt/C and Rh/C. As expected, the N-fcc-Rh-300 electrocatalyst exhibits extraordinary HzOR performance with a low working potential (−81 mV) at 10 mA cm<sup>−2</sup>, which is much lower than those of Tri-RhO<sub>2</sub> (−1 mV), Pt/C (78 mV) and Rh/C (98 mV) (Fig. 4b). Besides, N-fcc-Rh-300 also shows a small Tafel slope (14.1 mV dec<sup>−1</sup>), which is much lower than those of Tri-RhO<sub>2</sub> (47.1 mV dec<sup>−1</sup>), Pt/C (62.2 mV dec<sup>−1</sup>) and Rh/C (72.5 mV dec<sup>−1</sup>), suggesting its favorable catalytic kinetics and fast

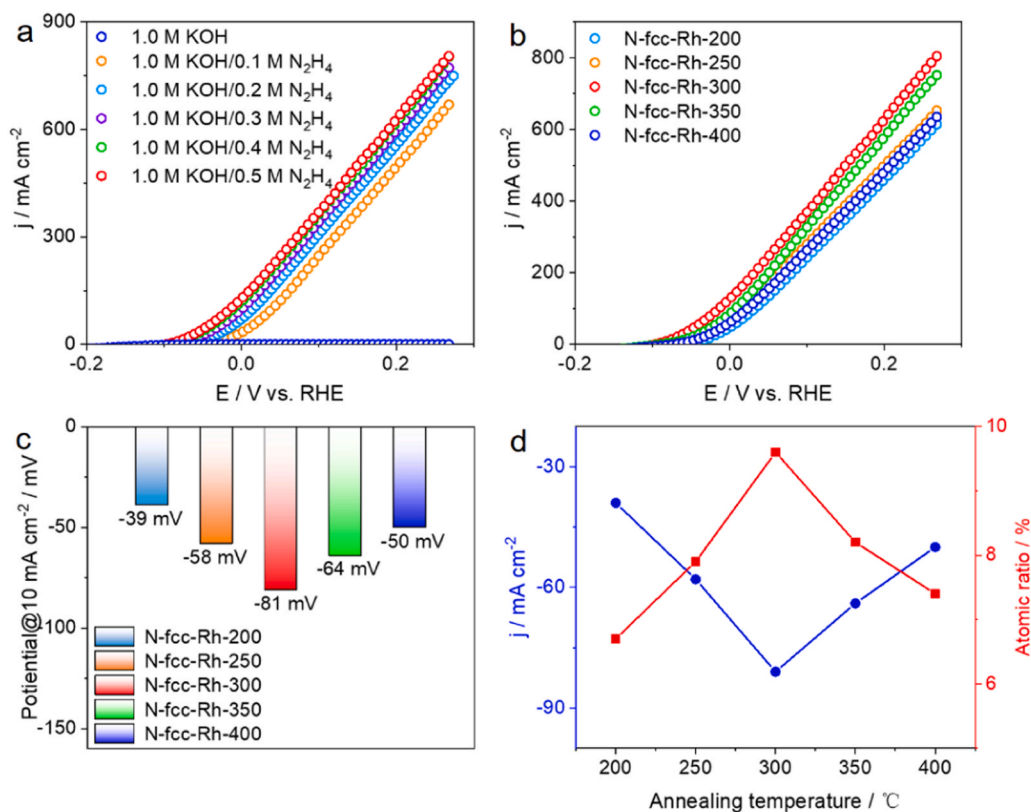


Fig. 3. (a) Polarization curves of N-fcc-Rh-300 in different concentrations of  $\text{N}_2\text{H}_4$  toward HzOR process. (b) HzOR polarization curves; (c) Comparison of the working potential of N-fcc-Rh with different annealing temperatures. (d) The changes of N/Rh atomic ratio and working potentials at the current density of  $-10 \text{ mA cm}^{-2}$  with different annealing temperatures.

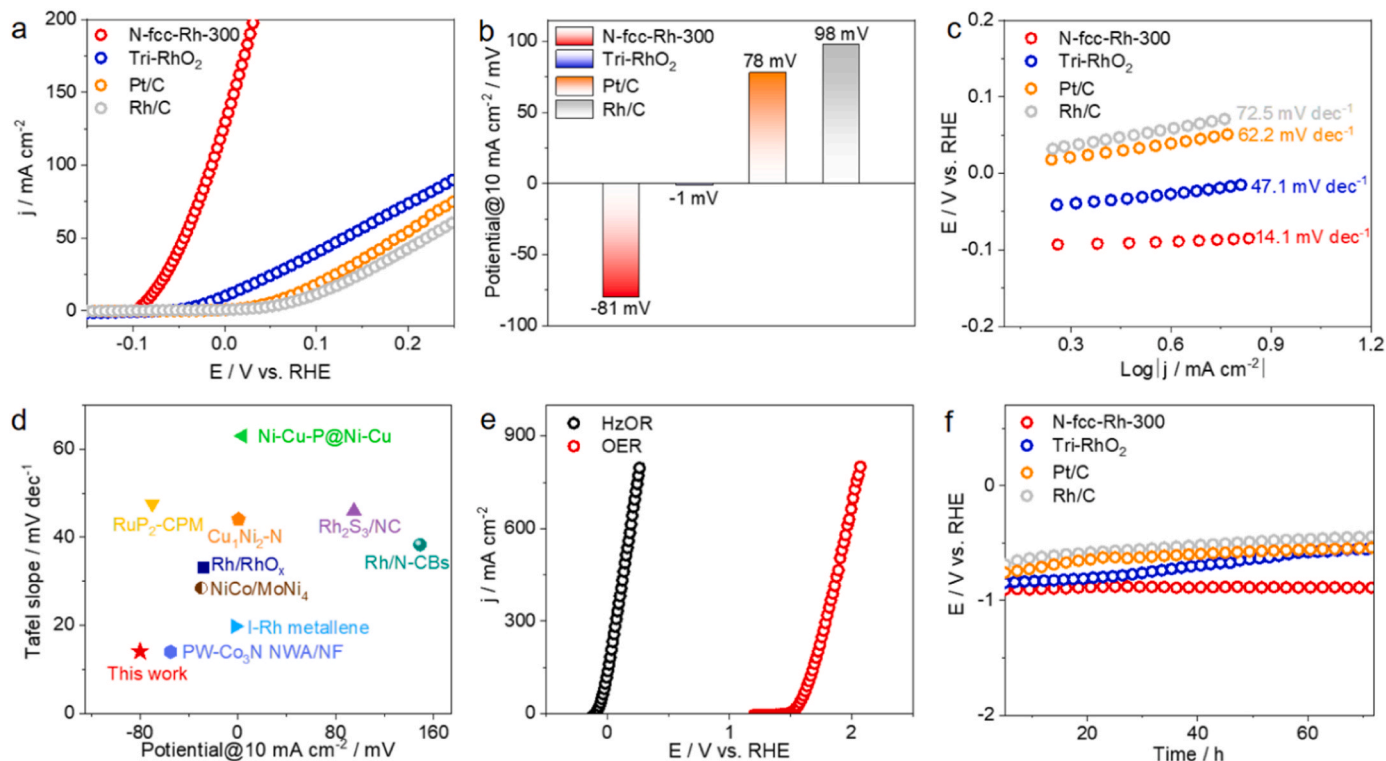


Fig. 4. (a) HzOR polarization curves of different samples. (b) Comparison of the working potential of different samples. (c) Tafel plots for different samples. (d) Comparison of working potentials and Tafel slopes for N-fcc-Rh-300 with previously reported HzOR catalysts (Rh/RhO<sub>x</sub> [53], RuP<sub>2</sub>-CPM [54], Rh/N-CBs [55], Rh<sub>2</sub>S<sub>3</sub>/NC [56], Cu<sub>1</sub>Ni<sub>2</sub>-N [18], I-Rh metallene [47], Ni-Cu-P @ Ni-Cu [57], PW-Co<sub>3</sub>N NWA/NF [58], NiCo/MoNi<sub>4</sub> [59]). (e) Polarization curves for the N-fcc-Rh-300 for HzOR and OER. (f) The long-term durability test of different samples with a constant current density of  $10 \text{ mA cm}^{-2}$ .



electron transfer toward HzOR (Fig. 4c) [49–51]. In addition, we also compare the HzOR activity of the optimal N-fcc-Rh-300 with previous reported efficient HzOR electrocatalysts, further reflecting its excellent HzOR activity (Fig. 4d and Table S1). As shown in Fig. 4e, the HzOR performance of the optimal N-fcc-Rh-300 electrocatalyst is a more energy-efficient process in comparison to its OER process. In addition to the activity, durability is another crucial factor in the practical application of electrocatalysts [52]. The chronopotentiometry test at  $10 \text{ mA cm}^{-2}$  was used to verify the durability of HzOR for N-fcc-Rh-300. During a 72 h of electrolysis, only slight potential decay can be observed as shown in Fig. 4f, demonstrating the superior electrocatalytic HzOR stability of the N-fcc-Rh-300 electrocatalyst. This superior durability also makes N-fcc-Rh-300 prevail over most reported electrocatalysts for HzOR under alkaline conditions (Table S2). As displayed in Fig. S13, the BET surface area of the N-fcc-Rh is determined to be  $11.12 \text{ m}^2 \text{ g}^{-1}$ . The electrochemical impedance spectroscopy (EIS) measurements of the N-fcc-Rh-300 before and after the stability test were also collected and displayed in Fig. S14, indicating the change of charge transfer resistance ( $R_{ct}$ ) is limited for the N-fcc-Rh-300 before and after the HzOR stability test. To further study the transformation of morphology and crystal structure of the N-fcc-Rh-300 electrocatalyst after a long-term HzOR stability test, the XRD, SEM, TEM, and EDX-mapping of N-fcc-Rh-300 after the stability test is collected and displayed in Fig. S15. The XRD pattern indicates almost no change in the crystal structure for N-fcc-Rh after the stability test (Fig. S15a). SEM and TEM images reveal that the 2D morphology of N-fcc-Rh was still well preserved after the stability test (Figs. S15b and S15c). After the stability test, EDX-mapping images show that Rh and N elements are still evenly distributed in the nano-sheets (Figs. S15d, S15e and S15f). The EDX elemental analysis and XPS spectra of N-fcc-Rh-300 also showed negligible changes (Figs. S16 and S17).

Moreover, the hydrogen evolution reaction (HER) activity of the optimal N-fcc-Rh-300 was also evaluated in the  $1.0 \text{ M KOH}$  electrolyte.

As shown in Fig. 5a, the HER activity of N-fcc-Rh-300 is almost the same as that of Pt/C. Specifically, the overpotentials of N-fcc-Rh-300 and Pt/C are determined to be  $60 \text{ mV}$  and  $56 \text{ mV}$  at  $-10 \text{ mA cm}^{-2}$ , respectively. Inspired by the excellent HER and HzOR activity of N-fcc-Rh-300, overall hydrazine splitting (OHZS) was assembled using the N-fcc-Rh-300 as both anode and cathode electrode materials in the  $1.0 \text{ M KOH}/0.5 \text{ M N}_2\text{H}_4$  electrolyte. Fig. 5b shows the schematic illustration of the process. To highlight the comparison, the overall water splitting (OWS) is measured without  $\text{N}_2\text{H}_4$ . The comparing LSV curves of OWS and OHZS are illustrated in Fig. 5c. As expected, the polarization curve indicates that the OHZS exhibits a higher current density than the OWS at the same applied potential. Precisely, it only requires cell voltages of  $0.197$ ,  $0.481$ ,  $0.759$ , and  $0.999 \text{ V}$  in the OHZS system to afford  $10$ ,  $50$ ,  $100$ , and  $200 \text{ mA cm}^{-2}$ , whereas the OWS system requires much higher values of  $1.855$ ,  $2.212$ ,  $2.487$  and  $2.724 \text{ V}$ , respectively (Fig. 5d).

### 3.3. DFT calculations

To gain further insights into the catalytic mechanism, DFT calculations were employed to investigate the N-fcc-Rh catalyzed HzOR process. Specifically, both the clean Rh (111) surface and the N-fcc-Rh (111) surface were constructed and their reaction pathways for HzOR were studied, respectively (see more computations methods in SI, Fig. 6c). Our computational findings, as depicted in Fig. 6a, indicate that the potential determining step (PDS) for HzOR in both two materials occur during the initial deprotonation reaction of  $^*\text{NH}_2\text{NH}_2$  to form  $^*\text{NHNH}_2$ . Remarkably, the addition of nitrogen has a pronounced effect on lowering the free energy of the PDS on the N-fcc-Rh(111) surface compared to the Rh(111) surface, with an energy reduction of  $0.04 \text{ eV}$ , thus enhancing the overall efficiency of the HzOR reaction. Moreover, as illustrated in Fig. 6a, the N-fcc-Rh(111) catalyst exhibits improved performance in the final  $\text{N}_2$  desorption process compared to the Rh(111) surface, resulting in reduced susceptibility to catalyst poisoning.

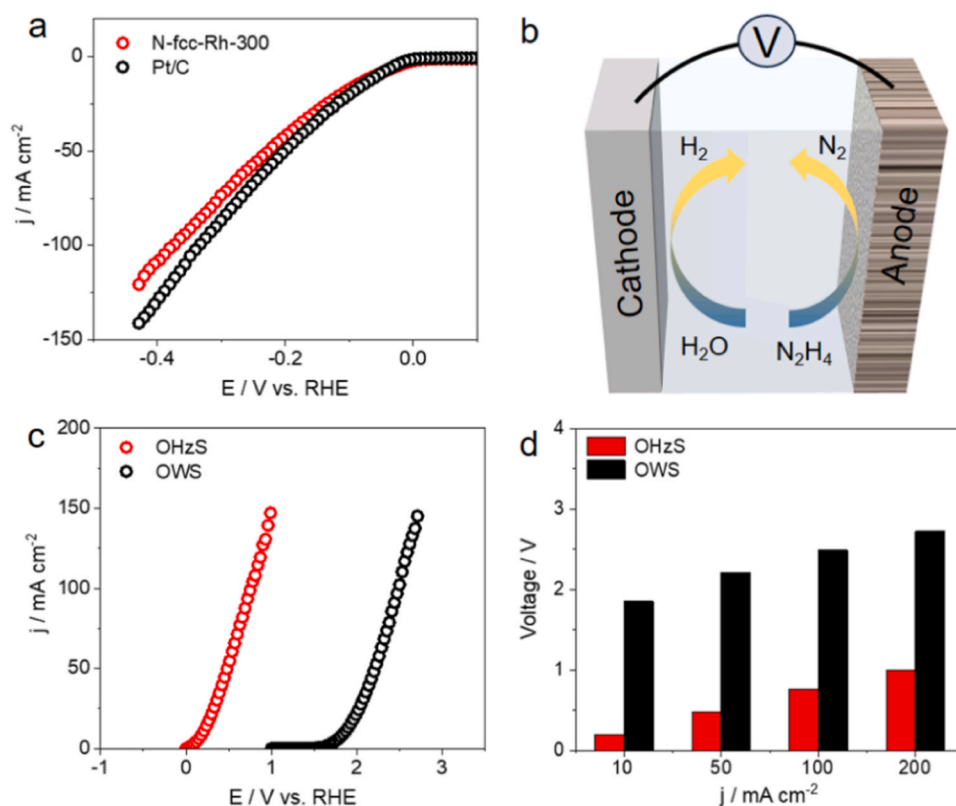


**Fig. 5.** (a) HER polarization curves of N-fcc-Rh-300 and Pt/C in  $1.0 \text{ M KOH}$  electrolyte. (b) Schematic representation of the hydrazine electrolyzer. (c) LSV curves for the OWS and the OHZS. (d) Comparing the cell voltage to achieve a  $10$ ,  $50$ ,  $100$  and  $200 \text{ mA cm}^{-2}$  for N-fcc-Rh-300.

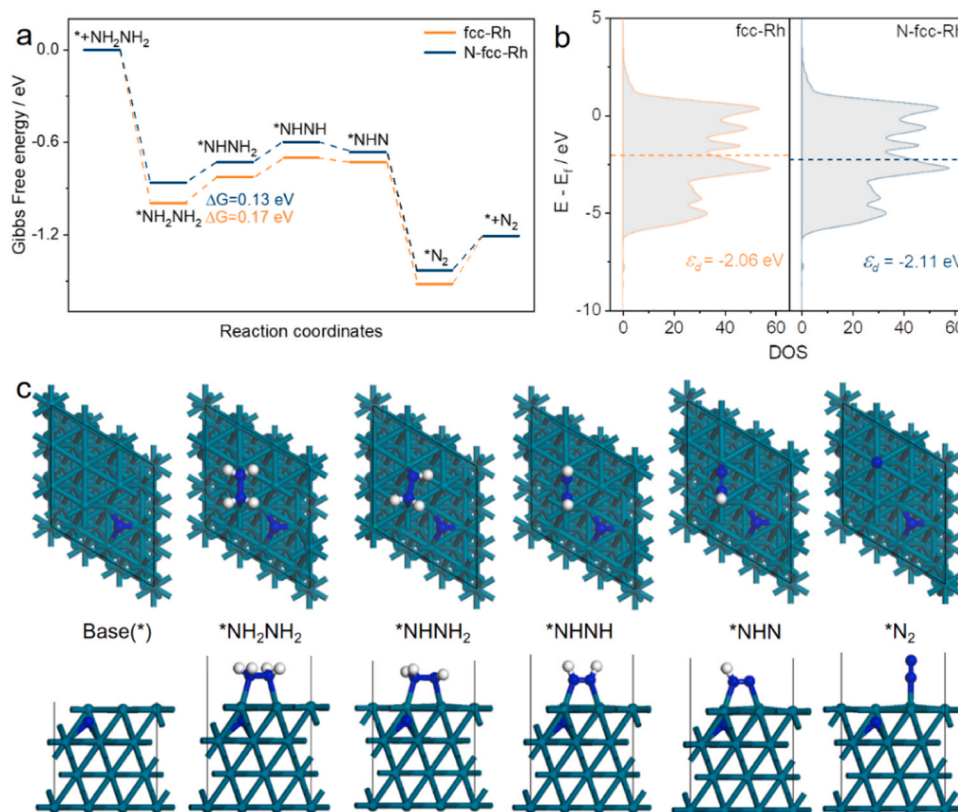


**Fig. 6.** (a) Free energy profiles and reaction pathways of HzOR on fcc-Rh and N-fcc-Rh. (b) the  $d$ -band center of fcc-Rh and N-fcc-Rh. (c) The simulation models of N-fcc-Rh for DFT calculations. The white, green and blue balls represent H, Rh, and N atoms, respectively.

Subsequent investigations of the  $d$ -band center (Figs. 6b and 6c) demonstrate that the addition of nitrogen induces a shift of the Rh  $d$ -band center away from the Fermi level by 0.05 eV, indicating a weakened strong interaction between  $\text{NH}_2\text{NH}_2$  and the adsorption site, thereby facilitating the dehydrogenation of  $^*\text{NH}_2\text{NH}_2$  to form  $^*\text{NHNH}_2$  [60]. In summary, our theoretical calculations suggest that the N-fcc-Rh (111) facilitates the HzOR process, which aligns well with experimental observations. These results provide valuable insights for understanding and designing more efficient catalysts for HzOR.

The schematic illustrating of HzOR mechanism for fcc-Rh and N-fcc-Rh is shown in Fig. 7. For fcc-Rh, the binding energy between Rh and  $^*\text{NH}_2\text{NH}_2$  is stronger, resulting in a larger formation energy of the PDS ( $^*\text{NH}_2\text{NH}_2 + \text{OH}^- \rightarrow ^*\text{NH}_2\text{NH} + \text{H}_2\text{O} + \text{e}^-$ ) (Fig. 7a). However, the binding energy between Rh and  $^*\text{NH}_2\text{NH}_2$  weakens after the addition of the N element, resulting in a decrease in the formation energy of the PDS (Fig. 7b). In addition, the N-fcc-Rh(111) catalyst further weakens the adsorption of poisons in the final  $\text{N}_2$  desorption process (Fig. S18), thereby enhancing the anti-poisoning effect. Therefore, it is feasible to

enhance the HzOR performance by adding the N elements.

#### 4. Conclusions

In summary, the N-fcc-Rh-300 nanosheets are prepared by directly annealing the Tri-RhO<sub>2</sub> precursor in the  $\text{NH}_3$  atmosphere. The 2D ultrathin nanostructures expose more active sites. Introducing the N element effectively tunes the electronic structure and accelerates the charge transfer, improving the electrocatalytic activity. The optimized N-fcc-Rh-300 electrocatalyst affords an outstanding HzOR electrocatalytic performance with a working potential of  $-81$  mV and a Tafel slope of  $14.1$  mV  $\text{dec}^{-1}$  at  $10$  mA  $\text{cm}^{-2}$ .

#### CRediT authorship contribution statement

**Fan Zhenglong:** Writing – review & editing. **Ma Mengjie:** Investigation. **Cheng Tao:** Investigation. **Zhu Wenxiang:** Investigation. **Chen Jinxin:** Investigation. **Sun Qintao:** Formal analysis, Writing – original

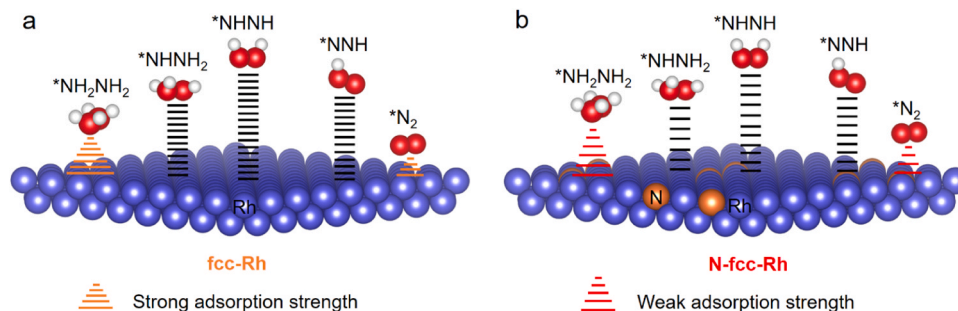


**Fig. 7.** The schematic illustrating of HzOR mechanism for (a) fcc-Rh and (b) N-fcc-Rh.

draft. **Shi Jie**: Conceptualization, Formal analysis, Writing – original draft. **Kang Zhenhui**: Funding acquisition, Supervision, Writing – review & editing. **Shao Mingwang**: Writing – review & editing. **Liao Fan**: Funding acquisition, Supervision, Writing – review & editing. **Yang Hao**: Writing – review & editing.

## Declaration of Competing Interest

The authors declare that they have no known competing financial interests or personal relationships that could have appeared to influence the work reported in this paper.

## Data availability

Data will be made available on request.

## Acknowledgements

This work is supported by Natural Science Foundation of Jiangsu Province (BK20220028), National MCF Energy R&D Program of China (2018YFE0306105), National Key R&D Program of China (2020YFA0406103), Innovative Research Group Project of the National Natural Science Foundation of China (51821002), National Natural Science Foundation of China (51972216, 52272043, 52271223, 52202107, 52201269, 22173066, 22103054, 61971143, 21903058, 22173066 and 22103054), Natural Science Foundation of Jiangsu Province (BK20210735, 21KJB430043), The Science and Technology Development Fund, Macau SAR (0009/2022/ITP), Collaborative Innovation Center of Suzhou Nano Science & Technology, the 111 Project, and Suzhou Key Laboratory of Functional Nano & Soft Materials.

## Appendix A. Supporting information

(1) Supplementary Figs. S1–S13; (2) Supplementary Tables S1–S2. Supplementary data associated with this article can be found in the online version at [doi:10.1016/j.apcatb.2023.123561](https://doi.org/10.1016/j.apcatb.2023.123561).

## References

- [1] F. Yu, Q.H. Deng, H.P. Li, Y.G. Xia, W.G. Hou, A general strategy to synthesize single-atom metal-oxygen doped polymeric carbon nitride with highly enhanced photocatalytic water splitting activity, *Appl. Catal. B* 323 (2023), 122180, <https://doi.org/10.1016/j.apcatb.2022.122180>.
- [2] M.C. Luo, Z.L. Zhao, Y.L. Zhang, Y.J. Sun, Y. Xing, F. Lv, Y. Yang, X. Zhang, S. Hwang, Y.N. Qin, J.Y. Ma, F. Lin, D. Su, G. Lu, S.J. Guo, PdMo bimetallic for oxygen reduction catalysis, *Nature* 574 (2019) 81–85, <https://doi.org/10.1038/s41586-019-1603-7>.
- [3] Y.F. Chen, H.L. Yao, F.T. Kong, H. Tian, G. Meng, S.Z. Wang, X.P. Mao, X.Z. Cui, X. M. Hou, J.L. Shi, V<sub>2</sub>C MXene synergistically coupling FeNi LDH nanosheets for boosting oxygen evolution reaction, *Appl. Catal. B* 297 (2021), 120474, <https://doi.org/10.1016/j.apcatb.2021.120474>.
- [4] K.Y. Zhu, X.F. Zhu, W.S. Yang, Application of in situ techniques for the characterization of NiFe-based oxygen evolution reaction (OER) electrocatalysts, *Angew. Chem. Int. Ed.* 58 (2019) 1252–1265, <https://doi.org/10.1002/anie.201802923>.
- [5] H.C.A. Sun, W. Zhang, J.G. Li, Z.S. Li, X. Ao, K.H. Xue, K.K. Ostrikov, J. Tang, C. D. Wang, Rh-engineered ultrathin NiFe-LDH nanosheets enable highly-efficient overall water splitting and urea electrolysis, *Appl. Catal. B* 284 (2021), 119740, <https://doi.org/10.1016/j.apcatb.2020.119740>.
- [6] X. Bo, R.K. Hocking, S. Zhou, Y.B. Li, X.J. Chen, J.C. Zhuang, Y. Du, C. Zhao, Capturing the active sites of multimetallic (oxy)hydroxides for the oxygen evolution reaction, *Energy Environ. Sci.* 13 (2020) 4225–4237, <https://doi.org/10.1039/D0EE01609H>.
- [7] X.F. Yang, L. Tian, X.L. Zhao, H. Tang, Q.Q. Liu, G.S. Li, Interfacial optimization of g-C<sub>3</sub>N<sub>4</sub>-based Z-scheme heterojunction toward synergistic enhancement of solar-driven photocatalytic oxygen evolution, *Appl. Catal. B* 244 (2019) 240–249, <https://doi.org/10.1016/j.apcatb.2018.11.056>.
- [8] Y. Zhu, J.H. Zhang, Q.Z. Qian, Y.P. Li, Z.Y. Li, Y. Liu, C. Xiao, G.Q. Zhang, Y. Xie, Dual nanoislands on Ni/C hybrid nanosheet activate superior hydrazine oxidation-assisted high-efficiency H<sub>2</sub> production, *Angew. Chem. Int. Ed.* 61 (2022), e202113082, <https://doi.org/10.1002/anie.202113082>.
- [9] Y.P. Li, J.M. Li, Q.Z. Qian, X. Jin, Y. Liu, Z.Y. Li, Y. Zhu, Y.M. Guo, G.Q. Zhang, Superhydrophilic Ni-based multicomponent nanorod-confined-nanoflake array electrode achieves waste-battery-driven hydrogen evolution and hydrazine oxidation, *Small* 17 (2021), 2008148, <https://doi.org/10.1002/smll.202008148>.
- [10] Y. Jeong, S.S. Naik, Y. Yu, J. Theerthagiri, S.J. Lee, P.L. Show, H.C. Choi, M. Y. Choi, Ligand-free monophase CuPd alloys endow boosted reaction kinetics toward energy-efficient hydrogen fuel production paired with hydrazine oxidation, *J. Mater. Sci. Technol.* 143 (2023) 20–29, <https://doi.org/10.1016/j.jmst.2022.09.043>.
- [11] X.H. Chen, H.C. Fu, L. Wu, X.L. Li, B. Yang, T. Li, F. Gu, J.L. Lei, N.B. Li, H.Q. Luo, Tuning the d-band center of NiC<sub>2</sub>O<sub>4</sub> with Nb<sub>2</sub>O<sub>5</sub> to optimize the Volmer step for hydrazine oxidation-assisted hydrogen production, *Green Chem.* 24 (2022) 5559–5569, <https://doi.org/10.1039/D2GC01158A>.
- [12] X.Y. Guan, Q.N. Wu, H.B. Li, S.Y. Zeng, Q.X. Yao, R. Li, H.Y. Chen, Y. Zheng, K. G. Qu, Identifying the roles of Ru single atoms and nanoclusters for energy-efficient hydrogen production assisted by electrocatalytic hydrazine oxidation, *Appl. Catal. B* 323 (2023), 122145, <https://doi.org/10.1016/j.apcatb.2022.122145>.
- [13] Z.Y. Wang, L. Xu, F.Z. Huang, L.B. Qu, J.T. Li, K.A. Owusu, Z. Liu, Z.F. Lin, B. H. Xiang, X. Liu, K.N. Zhao, X.B. Liao, W. Yang, Y.B. Cheng, L.Q. Mai, Copper-nickel nitride nanosheets as efficient bifunctional catalysts for hydrazine-assisted electrolytic hydrogen production, *Adv. Energy Mater.* 9 (2019), 1900390, <https://doi.org/10.1002/aenm.201900390>.
- [14] S. Sarker, J.H. Choi, H.H. Lee, D.S. Kim, H.K. Cho, Surface-confined ultra-low scale Pd engineered layered Co(OH)<sub>2</sub> toward high-performance hydrazine electrooxidation in alkaline saline water, *Adv. Sci.* 10 (2023), 2300639, <https://doi.org/10.1002/adv.202300639>.
- [15] Z.P. Yu, C.W. Si, F. Sabaté, A.P. LaGrow, Z.X. Tai, V.M. Diaconescu, L. Simonelli, L. J. Meng, M.J. Sabater, B. Li, L.F. Liu, Defective Ru-doped α-MnO<sub>2</sub> nanorods enabling efficient hydrazine oxidation for energy-saving hydrogen production via proton exchange membranes at near-neutral pH, *Chem. Eng. J.* 470 (2023), 144050, <https://doi.org/10.1016/j.cej.2023.144050>.
- [16] Q.Z. Qian, J.H. Zhang, J.M. Li, Y.P. Li, X. Jin, Y. Zhu, Y. Liu, Z.Y. Li, A. El-Harairy, C. Xiao, G.Q. Zhang, Y. Xie, Artificial heterointerfaces achieve delicate reaction kinetics towards hydrogen evolution and hydrazine oxidation catalysis, *Angew. Chem. Int. Ed.* 60 (2021) 5984–5993, <https://doi.org/10.1002/anie.202014362>.
- [17] S.C. Zhang, C.H. Zhang, X.S. Zheng, G. Su, H.L. Wang, M.H. Huang, Integrating electrophilic and nucleophilic dual sites on heterogeneous bimetallic phosphide via enhancing interfacial electronic field to boost hydrazine oxidation and hydrogen evolution, *Appl. Catal. B* 324 (2023), 122207, <https://doi.org/10.1016/j.apcatb.2022.122207>.
- [18] S.X. Zhuang, Y. Tang, X.F. Tai, Q. Huang, P.Y. Wan, Y.M. Chen, Y.Z. Sun, J.Q. Pan, X.J. Yang, Hydrogen and electricity co-generation from hydrazine-assisted water electrolysis on hierarchical porous heteroatoms-doped CoCu catalysts, *Appl. Catal. B* 306 (2022), 121132, <https://doi.org/10.1016/j.apcatb.2022.121132>.
- [19] Q. Liu, X.B. Liao, Y.H. Tang, J.H. Wang, X.Z. Lv, X.L. Pan, R.H. Lu, Y. Zhao, X.Y. Yu, H.B. Wu, Low-coordinated cobalt arrays for efficient hydrazine electrooxidation, *Energy Environ. Sci.* 15 (2022) 3246–3256, <https://doi.org/10.1039/d2ee01463g>.
- [20] F. Sun, J.S. Qin, Z.Y. Wang, M.Z. Yu, X.H. Wu, X.M. Sun, J.S. Qiu, Energy-saving hydrogen production by chlorine-free hybrid seawater splitting coupling hydrazine degradation, *Nat. Commun.* 12 (2021), 4182, <https://doi.org/10.1038/s41467-021-24529-3>.
- [21] P. Shen, B.W. Zhou, Z. Chen, W.P. Xiao, Y.L. Fu, J. Wan, Z.X. Wu, L. Wang, Ruthenium-doped 3D Cu<sub>2</sub>O nanochains as efficient electrocatalyst towards hydrogen evolution and hydrazine oxidation, *Appl. Catal. B* 325 (2023), 122305, <https://doi.org/10.1016/j.apcatb.2022.122305>.
- [22] Y. Yu, S.J. Lee, J. Theerthagiri, Y. Lee, M.Y. Choi, Architecting the AuPt alloys for hydrazine oxidation as an anolyte in fuel cell: comparative analysis of hydrazine splitting and water splitting for energy-saving H<sub>2</sub> generation, *Appl. Catal. B* 316 (2022), 121603, <https://doi.org/10.1016/j.apcatb.2022.121603>.
- [23] T. Cui, J.Q. Chi, J.W. Zhu, X.M. Sun, J.P. Lai, Z.J. Li, L. Wang, Tuning the size and chemisorption of FeP<sub>4</sub> by trace Ru doping for hydrazine-assisted hydrogen evolution in seawater at large-current-density, *Appl. Catal. B* 319 (2022), 121950, <https://doi.org/10.1016/j.apcatb.2022.121950>.
- [24] J.H. Lee, D.Y. Jo, J.W. Choung, C.H. Kim, H.C. Ham, K.Y. Lee, Roles of noble metals (M = Ag, Au, Pd, Pt and Rh) on CeO<sub>2</sub> in enhancing activity toward soot oxidation: active oxygen species and DFT calculations, *J. Hazard. Mater.* 403 (2021), 124085, <https://doi.org/10.1016/j.jhazmat.2020.124085>.
- [25] W.S. Ni, X.J. Mao, H.L. Zhang, L. Liu, X.R. Guo, Q.L. Sun, Simultaneous determination of ultra-trace Pt, Pd, Rh and Ir in geochemical samples by inductively coupled plasma mass spectrometry following tin fire assay preconcentration and microwave digestion, *Curr. Anal. Chem.* 17 (2021) 552–563, <https://doi.org/10.2174/1573411016999200715160650>.
- [26] J.Y. Zhu, S.Q. Chen, Q. Xue, F.M. Li, H.C. Yao, L. Xu, Y. Chen, Hierarchical porous Rh nanosheets for methanol oxidation reaction, *Appl. Catal. B* 264 (2020), 118520, <https://doi.org/10.1016/j.apcatb.2019.118520>.
- [27] G.S. Hwang, W. Shin, G. Yim, J.H. Choi, Y.K. Kim, H. Jang, Y.R. Kim, Morphology-controlled silver-containing rhodium nanoparticles for the hydrogen evolution reaction, *J. Electrochem. Soc.* 169 (2022), 044517, <https://doi.org/10.1149/1945-7111/ac63f5>.
- [28] D. Liu, Z.J.J. Zhu, J.N. Li, L.W. Chen, H.Z. Huang, X.T. Jing, A.X. Yin, Rh-Cu alloy nano-dendrites with enhanced electrocatalytic ethanol oxidation activity, *J. Energy Chem.* 82 (2023) 343–349, <https://doi.org/10.1016/j.jechem.2023.03.038>.
- [29] Y. Zhao, N. Jia, X.R. Wu, F.M. Li, P. Chen, P.J. Jin, S.W. Yin, Y. Chen, Rhodium phosphide ultrathin nanosheets for hydrazine oxidation boosted electrochemical water splitting, *Appl. Catal. B* 270 (2020), 118880, <https://doi.org/10.1016/j.apcatb.2020.118880>.
- [30] T. Bian, B.B. Xiao, B. Sun, L. Huang, S. Su, Y. Jiang, J.K. Xiao, A.H. Yuan, H. Zhang, D.R. Yang, Local epitaxial growth of Au-Rh core-shell star-shaped decahedra: a



- case for studying electronic and ensemble effects in hydrogen evolution reaction, *Appl. Catal. B* 263 (2020), 118255, <https://doi.org/10.1016/j.apcatb.2019.118255>.
- [31] B.T. Sneed, C.N. Brodsky, C.H. Kuo, L.K. Lamontagne, Y. Jiang, Y. Wang, F. Tao, W. X. Huang, C.K. Tsung, Nanoscale-phase-separated Pd-Rh boxes synthesized via metal migration: an archetype for studying lattice strain and composition effects in electrocatalysis, *J. Am. Chem. Soc.* 135 (2013) 14691–14700, <https://doi.org/10.1021/ja405387q>.
- [32] J. Shi, Q.T. Sun, W.X. Zhu, T. Cheng, F. Liao, M.J. Ma, J.J. Yang, H. Yang, Z.L. Fan, M.W. Shao, Lattice strain dominated hydrazine oxidation reaction in single-metal-element nanosheet, *Chem. Eng. J.* 463 (2023), 142385, <https://doi.org/10.1016/j.cej.2023.142385>.
- [33] J.Y. Wang, W.T. Liu, X.P. Li, T. Ouyang, Z.Q. Liu, Strong hydrophilicity NiS<sub>2</sub>/Fe<sub>3</sub>S<sub>4</sub> heterojunctions encapsulated in N-doped carbon nanotubes for enhanced oxygen evolution reaction, *Chem. Commun.* 56 (2020) 1489–1492, <https://doi.org/10.1039/c9cc09303f>.
- [34] H. Wan, X. Xiao, W. Ma, Y. Zhang, X.H. Liu, Y.Y. Liu, G. Chen, N. Zhang, Y.J. Cao, R.Z. Ma, Electronic configuration modulation of tin dioxide by phosphorus dopant for pathway change in electrocatalytic water oxidation, *Inorg. Chem. Front.* 9 (2022) 83–89, <https://doi.org/10.1039/D1QI01169C>.
- [35] S. Geng, Y. Ji, S. Yang, J. Su, Z. Hu, T.S. Chan, H. Yu, Y. Li, Y.Y. Chin, X. Huang, Q. Shao, Phosphorus optimized metastable hexagonal-close-packed phase nickel for efficient hydrogen peroxide production in neutral media, *Adv. Funct. Mater.* 33 (2023), 2300636, <https://doi.org/10.1002/adfm.202300636>.
- [36] L.F. Xiong, B. Wang, H.R. Cai, H.J. Hao, J. Li, T. Yang, S.C. Yang, Understanding the doping effect on hydrogen evolution activity of transition-metal phosphides: modeled with Ni<sub>2</sub>P, *Appl. Catal. B* 295 (2021), 120283, <https://doi.org/10.1016/j.apcatb.2021.120283>.
- [37] J.T. Ren, C.Y. Wan, T.Y. Pei, X.W. Lv, Z.Y. Yuan, Promotion of electrocatalytic nitrogen reduction reaction on N-doped porous carbon with secondary heteroatoms, *Appl. Catal. B* 266 (2020), 118633, <https://doi.org/10.1002/sml.202102363>.
- [38] F. Xiao, Z.P. Lin, J.K. Zhang, Y. Lei, Y. Meng, X.H. Chen, S.L. Zhao, B. Hong, J. Wang, D.Y. Li, J.T. Xu, A novel approach to facile synthesis of boron and nitrogen co-doped graphene and its application in lithium oxygen batteries, *Energy Storage Mater.* 41 (2021) 61–68, <https://doi.org/10.1016/j.ensm.2021.05.042>.
- [39] Y.J. Zhou, F. Liao, Y. Liu, Z.H. Kang, The advanced multi-functional carbon dots in photoelectrochemistry based energy conversion, *Int. J. Extrem. Manuf.* 4 (2022), 042001, <https://doi.org/10.1088/2631-7990/ac8e3a>.
- [40] Z.L. Fan, F. Liao, Y.J. Ji, Y. Liu, H. Huang, D. Wang, K. Yin, H.W. Yang, M.J. Ma, W. X. Zhu, M. Wang, Z.H. Kang, Y.Y. Li, M.W. Shao, Z.W. Hu, Q. Shao, Coupling of nanocrystal hexagonal array and two-dimensional metastable substrate boosts H<sub>2</sub> production, *Nat. Commun.* 13 (2022), 5828, <https://doi.org/10.1038/s41467-022-33512-5>.
- [41] X.W. Zhong, J. Tang, J.W. Wang, M.M. Shao, J.W. Chai, S.P. Wang, M. Yang, Y. Yang, N. Wang, S.J. Wang, B.M. Xu, H. Pan, 3D heterostructured pure and N-Doped Ni<sub>3</sub>S<sub>2</sub>/VS<sub>2</sub> nanosheets for high efficient overall water splitting, *Electrochim. Acta* 269 (2018) 55–61, <https://doi.org/10.1016/j.electacta.2018.02.131>.
- [42] Q.Q. Mao, K. Deng, W.X. Wang, P. Wang, Y. Xu, Z.Q. Wang, X.N. Li, L. Wang, H. J. Wang, N-doping induced lattice-strained porous PdIr bimetallic for pH-universal hydrogen evolution electrocatalysis, *J. Mater. Chem. A* 10 (2022) 8364–8370, <https://doi.org/10.1039/d2ta00590e>.
- [43] Y. Wei, J.J. Fu, H. Song, B. Zhang, C.R. Pi, L. Xia, X.M. Zhang, B. Gao, Y. Zheng, P. K. Chu, N-doped TiO<sub>2</sub> nanotube arrays with uniformly embedded Co<sub>x</sub>P nanoparticles for high-efficiency hydrogen evolution reaction, *RSC Adv.* 9 (2019) 11676–11682, <https://doi.org/10.1039/c9ra01184f>.
- [44] W. Chen, H. Wang, L.Q. Mao, X.P. Chen, W.F. Shangguan, Influence of loading Pt, RhO<sub>2</sub> co-catalysts on photocatalytic overall water splitting over H<sub>1.9</sub>K<sub>0.3</sub>La<sub>0.5</sub>Bi<sub>0.1</sub>Ta<sub>0.7</sub>O<sub>7</sub>, *Catal. Commun.* 57 (2014) 115–118, <https://doi.org/10.1016/j.catcom.2014.08.007>.
- [45] J.H. Tong, Y.L. Li, L.L. Bo, W.Y. Li, T. Li, Q. Zhang, D.Y. Kong, H. Wang, C.Y. Li, CoP/N-Doped carbon hollow spheres anchored on electrospinning core-shell N-Doped carbon nanofibers as efficient electrocatalysts for water splitting, *ACS Sustain. Chem. Eng.* 7 (2019) 17432, <https://doi.org/10.1021/acssuschemeng.9b04643>.
- [46] A.K. Sun, Y.L. Shen, Z.Z. Wu, D.Z. Wang, N-doped MoP nanoparticles for improved hydrogen evolution, *Int. J. Hydrog. Energy* 42 (2017) 14566–14571, <https://doi.org/10.1016/j.ijhydene.2017.04.122>.
- [47] S.Z. Geng, Y.J. Ji, S.Z. Yang, J.Q. Su, Z.W. Hu, T.S. Chan, H. Yu, Y.Y. Li, Y.Y. Chin, X.Q. Huang, Q. Shao, Phosphorus optimized metastable hexagonal-close-packed phase nickel for efficient hydrogen peroxide production in neutral media, *Adv. Funct. Mater.* 33 (2023), <https://doi.org/10.1002/adfm.202300636>.
- [48] K. Deng, Q.Q. Mao, W.X. Wang, P. Wang, Z.Q. Wang, Y. Xu, X.N. Li, H.J. Wang, L. Wang, Defect-rich low-crystalline Rh metallene for efficient chlorine-free H<sub>2</sub> production by hydrazine-assisted seawater splitting, *Appl. Catal. B* 310 (2022), 121338, <https://doi.org/10.1016/j.apcatb.2022.121338>.
- [49] H. Shen, T.R. Wei, Q. Liu, S.S. Zhang, J. Luo, X.J. Liu, Heterogeneous Ni-MoN nanosheet-assembled microspheres for urea-assisted hydrogen production, *Science* 374 (2023) 730–736, <https://doi.org/10.1016/j.jcis.2022.12.067>.
- [50] J.R. Hou, X.Y. Peng, J.Q. Sun, S.S. Zhang, Q. Liu, X.Z. Wang, J. Luo, X.J. Liu, Accelerating hydrazine-assisted hydrogen production kinetics with Mn dopant modulated CoS<sub>2</sub> nanowire arrays, *Inorg. Chem. Front.* (12) (2022) 3047–3058, <https://doi.org/10.1039/d2qi00083k>.
- [51] G. Meng, M.M. Jin, T.R. Wei, Q. Liu, S.S. Zhang, X.Y. Peng, J. Luo, X.J. Liu, MoC nanocrystals confined in N-doped carbon nanosheets toward highly selective electrocatalytic nitric oxide reduction to ammonia, *Nano Res.* (10) (2022) 8890–8896, <https://doi.org/10.1007/s12274-022-4747-y>.
- [52] T. Takahashi, Y. Kokubo, K. Murata, O. Hotaka, S. Hasegawa, Y. Tachikawa, M. Nishihara, J. Matsuda, T. Kitahara, S.M. Lyth, A. Hayashi, K. Sasaki, Cold start cycling durability of fuel cell stacks for commercial automotive applications, *Int. J. Hydrog. Energy* 47 (2022) 41111–41123, <https://doi.org/10.1016/j.ijhydene.2022.09.172>.
- [53] J.J. Yang, L. Xu, W.X. Zhu, M. Xie, F. Liao, T. Cheng, Z.H. Kang, M.W. Shao, Rh/RhO<sub>x</sub> nanosheets as pH-universal bifunctional catalysts for hydrazine oxidation and hydrogen evolution reactions, *J. Mater. Chem. A* 10 (2022) 1891–1898, <https://doi.org/10.1039/d1ta09391f>.
- [54] Y.P. Li, J.H. Zhang, Y. Liu, Q.Z. Qian, Z.Y. Li, Y. Zhu, G.Q. Zhang, Partially exposed RuP<sub>2</sub> surface in hybrid structure endows its bifunctionality for hydrazine oxidation and hydrogen evolution catalysis, *Sci. Adv.* 6 (2020), eabb4197, <https://doi.org/10.1126/sciadv.abb4197>.
- [55] N. Jia, Y.P. Liu, L. Wang, P. Chen, X.B. Chen, Z.W. An, Y. Chen, 0.2 V electrolysis voltage-driven alkaline hydrogen production with nitrogen-doped carbon nanobowl-supported ultrafine Rh nanoparticles of 1.4 nm, *ACS Appl. Mater. Interfaces* 11 (2019) 35039–35049, <https://doi.org/10.1021/acsaami.9b13586>.
- [56] C.X. Zhang, H.X. Liu, Y.F. Liu, X.J. Liu, Y.Y. Mi, R.J. Guo, J.Q. Sun, H.H. Bao, J. He, Y. Qiu, J.Q. Ren, X.J. Yang, J. Luo, G.Z. Hu, Rh<sub>2</sub>S<sub>3</sub>/N-doped carbon hybrids as pH-universal bifunctional electrocatalysts for energy-saving hydrogen evolution, *Small Methods* 4 (2020), 2000208, <https://doi.org/10.1002/smt.202000208>.
- [57] G.B. Darband, N. Lotfi, A. Aliabadi, S. Hyun, S. Shanmugam, Hydrazine-assisted electrochemical hydrogen production by efficient and self-supported electrodeposited Ni-Cu-P@Ni-Cu nano-micro dendrite catalyst, *Electrochim. Acta* 382 (2021), 138335, <https://doi.org/10.1016/j.electacta.2021.138335>.
- [58] Y. Liu, J.H. Zhang, Y.P. Li, Q.Z. Qian, Z.Y. Li, Y. Zhu, G.Q. Zhang, Manipulating dehydrogenation kinetics through dual-doping Co<sub>3</sub>N electrode enables highly efficient hydrazine oxidation assisting self-powered H<sub>2</sub> production, *Nat. Commun.* 11 (1) (2020) 13, <https://doi.org/10.1038/s41467-020-15563-8>.
- [59] Q.Z. Qian, Y.P. Li, Y. Liu, Y.M. Guo, Z.Y. Li, Y. Zhu, G.Q. Zhang, Hierarchical multi-component nanosheet array electrode with abundant NiCo/MoNi<sub>4</sub> heterostructure interfaces enables superior bifunctionality towards hydrazine oxidation assisted energy-saving hydrogen generation, *Chem. Eng. J.* 414 (2021), 128818, <https://doi.org/10.1016/j.cej.2021.128818>.
- [60] J.B. Ma, G.M. Zhong, P.R. Shi, Y.P. Wei, K.K. Li, L.K. Chen, X.G. Hao, Q.D. Li, K. Yang, C.R. Wang, W. Lv, Q.H. Yang, Y.B. He, F.Y. Kang, Constructing a highly efficient "solid-polymer-solid" elastic ion transport network in cathodes activates the room temperature performance of all-solid-state lithium batteries, *Energy Environ. Sci.* 15 (2022) 1503–1511, <https://doi.org/10.1039/D1EE03345J>.